Journal of Alloys and Compounds 846 (2020) 155987

Contents lists available at ScienceDirect

Journal of Alloys and Compounds

journal homepage: http://www.elsevier.com/locate/jalcom

Electronic structures and bonding of graphdiyne and its BN analogs: Transition from quasi-planar to planar sheets

İskender Muz [a, *], Mustafa Kurban [b]

[a] Department of Mathematics and Science Education, Nevşehir Hacı Bektaş Veli University, 50300, Nevşehir, Turkey
[b] Department of Electronics and Automation, Kırşehir Ahi Evran University, 40100, Kırşehir, Turkey

ARTICLE INFO

Article history:
Received 8 May 2020
Received in revised form
5 June 2020
Accepted 6 June 2020
Available online 9 June 2020

Keywords:
Graphdiyne
BNdiyne
Structural transition
Bonding
DFT

ABSTRACT

We demonstrate a possible structural transition from graphdiyne (GDY) to boron nitride (BN)-diyne ($C_{90-18n}(BN)_{9n}H_{18}$; $n = 0$-5) sheets using the density functional theory (DFT). The aim of this study is to investigate the effects of substitution of carbon atoms by B and N atoms on structural, electronic and reactivity properties. We found that a structural transition from quasi-planar to planar occurs at $n = 2$. The stability decreases with increasing the number of B/N. Moreover, the pristine BNdiyne is only less stable than pristine GDY by about 0.92 eV/atom. Our calculations also show that the energy gap (E_g) of the GDY and its BN structural analog models changes in the wide range of 0.45–5.52 eV as the number of B and N atoms increases in the system. The E_g of the BNdiyne ($n = 5$) is found to be 5.52 eV, indicating electrically an insulating behavior, however, it is 0.45 eV for the BNdiyne ($n = 4$) which is higher conductivity than that of pristine GDY. Molecular dynamics simulations show that temperature induces a decrease in the E_g due to variations of the bond energy and deformation in the structures under heat treatment. The ELF analysis also confirms that the B–N bonds in new GDY-like BN sheets potentially exhibit covalent characteristics. Our results herein show that new BNdiyne sheets can be used in promising applications from chemical nanosensors to solar cell applications.

© 2020 Elsevier B.V. All rights reserved.

1. Introduction

Graphdiyne (GDY), which has unique two-hybrid state (sp-sp^2), uniform pores, and highly π-conjugated structure [1,2], has attracted intense scrutiny in diverse fields of applications such as lithium-ion storage [3], nanocomposite photocatalyst [4], the anode of lithium and rechargeable batteries [5,6], clean energy [7], spintronics [8,9], and so on.

GDY, which has been grown on the surface of copper (Cu) via a cross-coupling reaction [10], is a novel 2D non-natural carbon allotrope containing hexagonal carbon rings connected by diacetylene bonds [1]. GDY exhibits high carrier mobility at room temperature owing to its bandgap of 0.46 eV [11,12]. GDY also has a high Seebeck coefficient, electrical conductivity and low thermal conductivity [13]. Based on the properties mentioned above, a GDY-based electrochemical actuator with a high electromechanical transduction efficiency of up to 6.03% was fabricated [14]. GDY electrode has recently been carried out for electrochemical supercapacitor [15]. The ultrathin GDY nanofilms significantly enhance the coulombic efficiency and long-term cycling performance of Li metal battery [16,17]. Besides, integrating ultrathin GDY sheets on silicon electrodes exhibited high-performance silicon anode [18]. The photocatalytic properties of a novel GDY-ZnO nanohybrid were examined on the degradation of methylene blue and rhodamine B [19].

Controlling and utilizing the electronic properties and chemical activities of carbon-based nanomaterials (CBNs) are a significant topic of research so that enhance the potential applications of them [20], doped with a foreign atom or molecule is an effective method [21–25]. Moreover, doping effects can be used to effectively adjust the electronic structures of CBNs. For example, the advances in the design of 2D-carbon nitride with dopant have been shown that it is possible to tune and control the energy gap of CBNs, thus change conductivity [26–31]. Among dopant atoms, in general, nitrogen (N)-and boron (B)-doped CBNs have been preferred, because the electrons can be injected into the materials by N atom [32] and thus tuning the electrical transport properties. In this context, N-doped CBNs have been extensively studied both theoretically and experimentally [33–37]. On the other hand, many studies show that N-

* Corresponding author.
E-mail address: iskendermuz@yahoo.com (İ. Muz).

https://doi.org/10.1016/j.jallcom.2020.155987
0925-8388/© 2020 Elsevier B.V. All rights reserved.

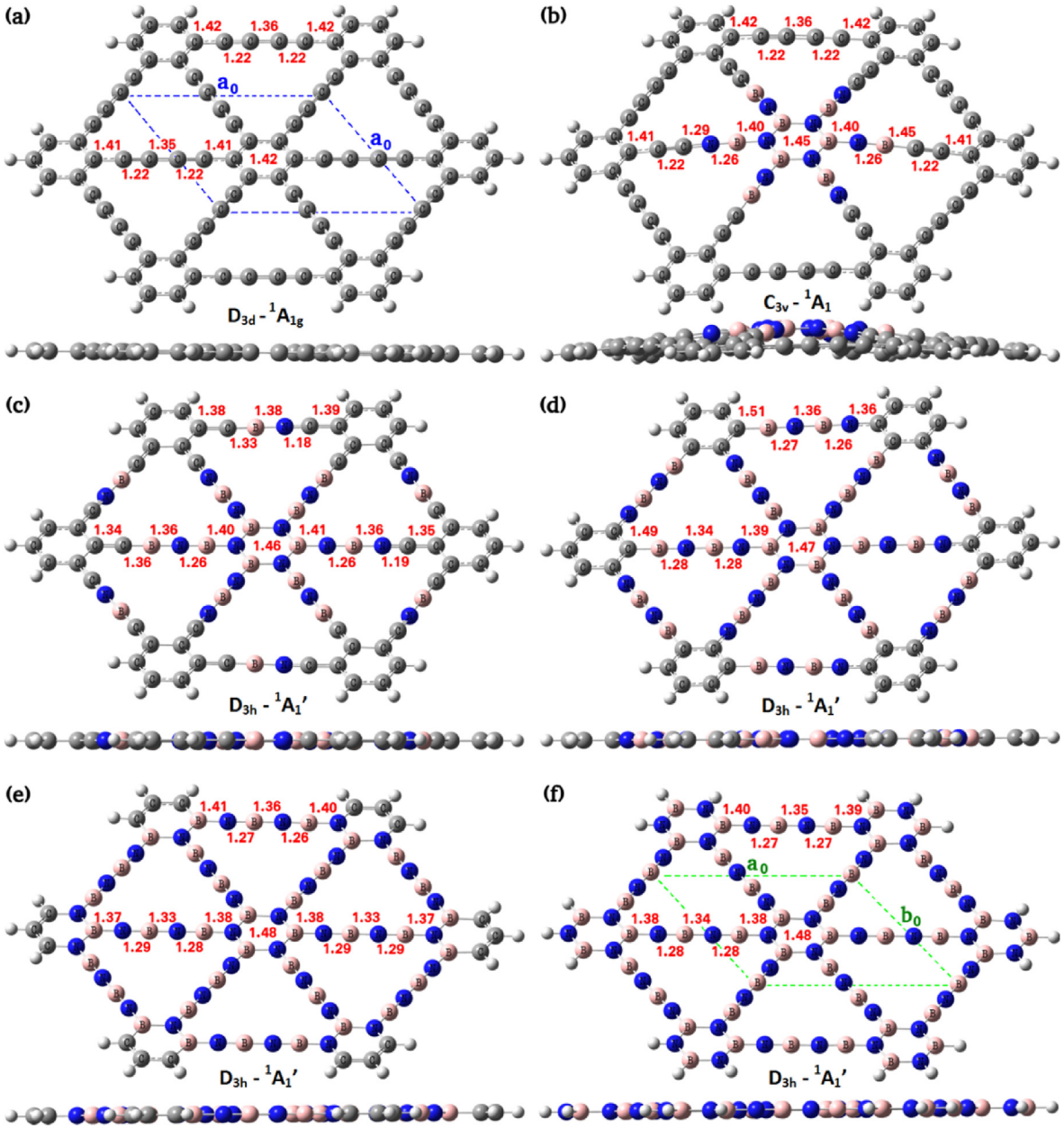

Fig. 1. (Colour online) The optimized geometries $n = 0$ **(a)**, $n = 1$ **(b)**, $n = 2$ **(c)**, $n = 3$ **(d)**, $n = 4$ **(e)** and $n = 5$ **(f)** for $C_{90\text{-}18n}(BN)_{9n}H_{18}$ models computed at B3LYP/6-31G(d) level of theory. (For interpretation of the references to colour in this figure legend, the reader is referred to the Web version of this article.)

doped GDY has more desirable properties than undoped GDY. For example, dopant N gives rise to an increase in the performance of GDY electrochemical electrodes for new energy fields, such as fuel cells, batteries, solar cells, Li/Na-ion capacitors [38,39]. Also, selectively N-doped GDY and porous GDY can be used as excellent metal-free catalysts for oxygen reduction [40,41]. A recent study showed the local structures of N-doped GDY based on computational X-ray spectroscopy [42]. On the other hand, B-GDY based materials are suggested as promising candidates for Li, Na and K ion batteries [43]. The motivation of the current work is to perform a systematic study on the transition from pristine graphdiyne (GDY) to BNdiyne ($C_{90\text{-}18n}(BN)_{9n}H_{18}$; $n = 0\text{-}5$) as novel two-dimensional BN sheets. Herein, we carried out the binding energy, formation energy, vertical ionization energy, vertical electron affinity, HOMO, LUMO, HOMO-LUMO energy gap, the density of state, charge distribution, electron localization function, Wiberg bond index, quantum chemical descriptors such as chemical hardness and potential, the maximum amount of electronic charge index, and electrophilicity index by density functional theory (DFT). The obtained energy gaps also compared with the long-range corrected (LC) self-consistent charge (SCC) density-functional based tight-binding (DFTB) and SCC-DFTB methods. Besides, molecular dynamics (MD) method was utilized to study the relationship between temperature and energy gap of the GDY and BNdiyne sheets.

2. Computational details

All the calculations have been performed using DFT calculations based on the reliable B3LYP exchange-correlation functional with an empirical dispersion term of Grimme's three-parameter (GD3 in

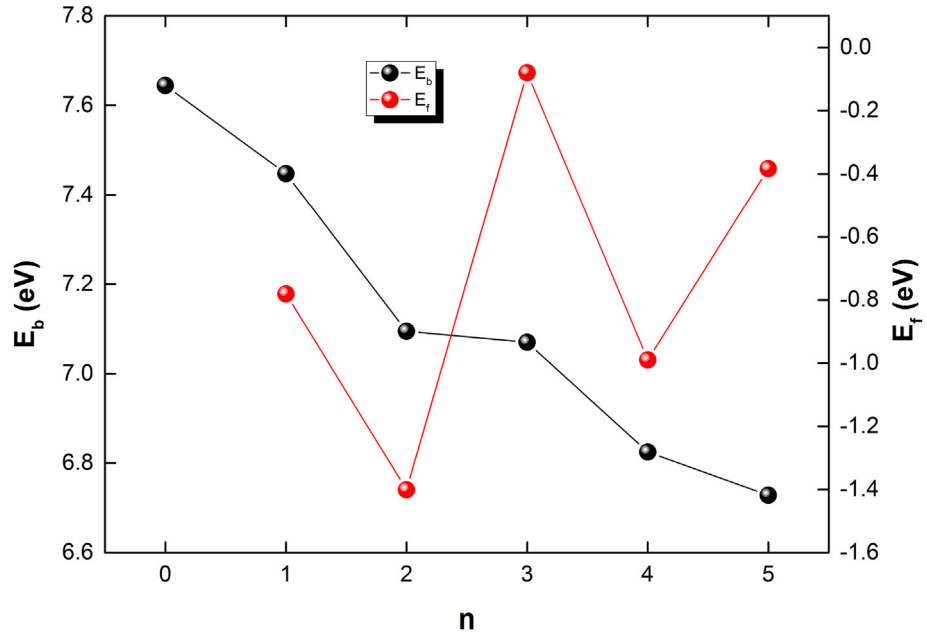

Fig. 2. (Colour online) The binding energy per atom(E_b) and formation energy (E_f) for $C_{90\text{-}18n}(BN)_{9n}H_{18}$ (n = *0-5*) models. (For interpretation of the references to colour in this figure legend, the reader is referred to the Web version of this article.)

Table 1
The electronic and reactivity properties of $C_{90\text{-}18n}(BN)_{9n}H_{18}$ (n = *0-5*) models. All values are eV.

	n					
	0	1	2	3	4	5
E_b	7.64	7.45	7.09	7.07	6.82	6.73
E_f	–	−0.78	−1.40	−0.08	−0.99	−0.38
VIP	6.20	6.18	5.18	6.25	2.98	7.21
VEA	2.10	1.80	2.39	0.54	2.28	0.20
HOMO	−5.46	−5.4	−4.51	−5.5	−3.94	−6.45
LUMO	−2.84	−2.56	−3.06	−1.96	−3.49	−0.93
E_g	2.62	2.84	1.45	3.54	0.45	5.52
η	1.31	1.42	0.73	1.77	0.23	2.76
Ωω	6.57	5.58	9.88	3.93	30.67	2.47
ΔN_{tot}	3.17	2.80	5.22	2.11	16.51	1.34

Gaussian 09) [44–46]. In addition, the 6-31G(d) basis set is selected to obtain the atomic orbitals for ensuring sufficiently accuracy and efficiency. We systematically investigated the transition from pristine graphdiyne (GDY) to BNdiyne ($C_{90\text{-}18n}(BN)_{9n}H_{18}$; n = *0-5*). Ends of pristine GDY were capped with hydrogen atoms to saturate dangling bonds due to fragment stabilization effect. GDY-like BN models were typically constructed by replacing 18 carbon atoms by 9 boron and 9 nitrogen atoms in pristine GDY ($C_{90}H_{18}$). This procedure continues until each C atom takes up the B and N atoms, and then all models were fully relaxed.

The binding energies E_b and formation energies E_f are calculated as follows:

$$E_b = (n_C \times E_C + n_B \times E_B + n_N \times E_N + n_H \times E_H - E_{total})/ \times (n_C + n_B + n_N + n_H) \quad (1)$$

$$E_f = E_{GDY} + (n_{B-incr.} \times E_B) + (n_{N-incr.} \times E_N) - (n_{C-decr.} \times E_C) - E_{BNdiyne} \quad (2)$$

where E_{total}, E_{GDY} and $E_{BNdiyne}$ are the total energies of GDY or its BN analogs. E_C, E_B E_N and E_H are the energies of C, B, N, and H atoms. n_C, n_N and n_H are the numbers of C, N and H atoms. The $n_{C-decr.}$, $n_{B-incr.}$ $n_{N-inc.}$ are the numbers of decreased C atoms and increased B/N atoms, respectively.

The vertical ionization potential (*VIP*) and vertical electron affinity (*VEA*) are calculated as follows: [$VIP = E^{cation} - E^{neutral}$] and [$VEA = E^{neutral} - E^{anion}$]. In these formulas, the *VIP* is defined as the difference between two energy levels the ground state of the cation (E^{cation}) and the ground state of the neutral ($E^{neutral}$) at the geometry of the neutral. The *VEA* is the difference between two energy levels the ground state of the neutral ($E^{neutral}$) and the ground state of the anion (E^{anion}) at the geometry of the neutral.

The HOMO and LUMO energies can be given with respect to Koopman's theorem by $I \approx -E_{HOMO}$ and $A \approx -E_{LUMO}$. In addition, chemical hardness (η), electrophilicity index (ω), maximum amount of electronic charge index (ΔN_{tot}) can be calculated as follows: [$\eta = (I - A)/2$], $\left[\omega = \left(\frac{(I+A)}{2}\right)^2/2\eta\right]$ and [$\Delta N_{tot} = -(I + A)/2\eta$].

GaussSum [47] and Multiwfn [48] programs are used to calculate the density of states (DOS), Wiberg bond index (WBI) and electron localization function (ELF), respectively. Besides, Gaussview [49] program is used for molecular structure visualizations. The obtained results are also compared with the LC−SCC−DFTB for GDY and SCC-DFTB methods implemented in DFTB + code [50]. MD simulations have been performed using DFTB with ob2-1-1/shift [51] and matsci [52] sets of Slater Koster parameters. The simulations use the Andersen thermostat [53] sampling an NVT ensemble. Verlet algorithm [54] was used for numerical integration with a time step length of 1 fs.

3. Results and discussions

As well as the point group symmetries and electronic states, the geometries of pristine GDY and its boron nitride (BN) analog models ($C_{90\text{-}18n}(BN)_{9n}H_{18}$; n = *0-5*) are completely optimized at the B3LYP/6-31G(d) level of theory and are presented in Fig. 1. Also, the

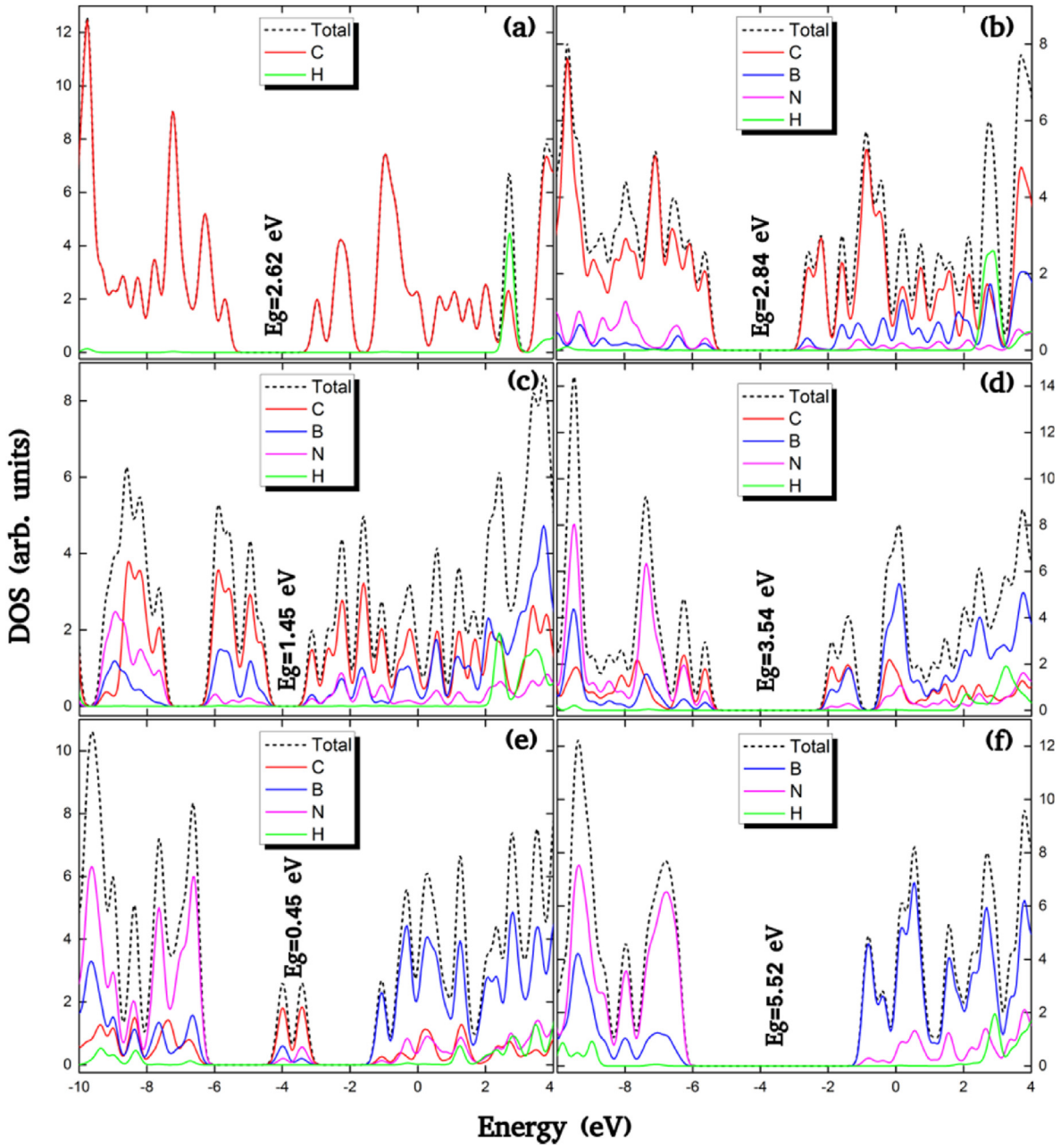

Fig. 3. (Colour online) Density of states (DOS) plots of $n = 0$ **(a)**, $n = 1$ **(b)**, $n = 2$ **(c)**, $n = 3$ **(d)**, $n = 4$ **(e)** and $n = 5$ **(f)** for $C_{90-18n}(BN)_{9n}H_{18}$ models. (For interpretation of the references to colour in this figure legend, the reader is referred to the Web version of this article.)

optimized cartesian coordinates of pristine GDY and its BN analogs are given in Tables S1–S6 (as Supporting Information).

$C_{90}H_{18}$ has a quasi-planar geometry with D_{3d} point group symmetry and $^1A_{1g}$ electronic state (see Fig. 1a). Bond types for the linking C–C bonds in $C_{90}H_{18}$ appear alternately as single (a single bond plus a delocalized p bond), double and triple bonds. The atomic framework of $C_{90}H_{18}$ can see to be C hexagon interconnected by acetylene $C \cdots C \equiv C - C \equiv C \cdots C$ chains. C–C bond distances along the chain are following: 1.41, 1.22, 1.35, 1.22, and 1.41 Å, whereas the C–C bond lengths in the C hexagon are larger, with an average value of 1.42 Å. This result is in excellent agreement with previous studies [55]. In addition, C–C bond lengths along the chains outside $C_{90}H_{18}$ are larger than those of towards center. When parallelogram with a broken (blue) line is plotted a unit cell (see Fig. 1a), the lattice constant of $C_{90}H_{18}$ is found to be $a_0 = 9.51$ Å, in good agreement with the previous values of 9.44–9.48 Å [11,56–60]. It can be easily seen when C atoms are replaced by B and N atoms, emerging models can be defined as BN analogs due to similarity with the GDY from view of topology. The first BN model ($n = 1$) is $C_{72}B_9N_9H_{18}$, has a quasi-planar geometry with C_{3v} point group symmetry and $^1A_1$ electronic state (see Fig. 1b). The atomic framework of $C_{72}B_9N_9H_{18}$ changes to be BN hexagon and so the geometry of $C_{90}H_{18}$ (GDY) is distorted when eighteen carbon atoms are replaced by nine B and nine N atoms. Interestingly, this replacement does not affect C–C bond distances in $C_{72}B_9N_9H_{18}$ model. B–N bond lengths in the hexagon ring are larger, with an average value of 1.45 Å than those of chains. In Fig. 1c-e, three BN models ($C_{54}B_{18}N_{18}H_{18}$; $n = 2$, $C_{36}B_{27}N_{27}H_{18}$; $n = 3$, and $C_{18}B_{36}N_{36}H_{18}$; $n = 4$) have a planar geometry with D_{3h} point group

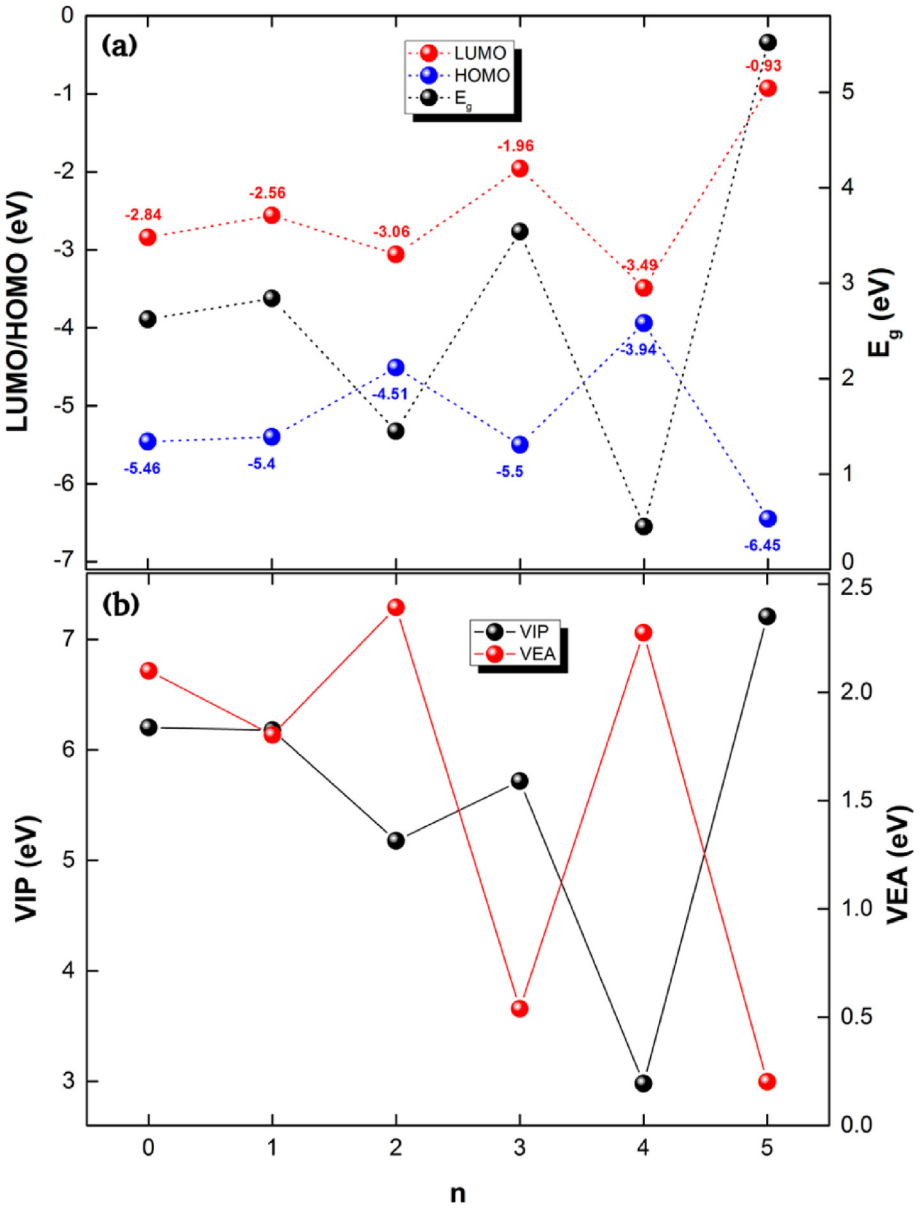

Fig. 4. (Colour online) LUMO, HOMO and HOMO-LUMO energy gap (E_g) **(a)**, vertical ionization potential (VIP) and vertical electron affinity (VEA) **(b)** for $C_{90-18n}(BN)_{9n}H_{18}$ ($n = 0$-5) models. (For interpretation of the references to colour in this figure legend, the reader is referred to the Web version of this article.)

symmetry and $^1A_1$' electronic state. It is note that a structural transition from quasi-planar (three-dimensional; 3D) to planar (two-dimensional; 2D) occurs in $C_{54}B_{18}N_{18}H_{18}$ (at $n = 2$). For $n = 2$, the shortest bond of 1.26 Å has a bond type of B(sp) = N(sp). Similarly, for $n = 3$-4, BN chains exhibit an approximate character of single and double bonds alternation. Moreover, it can be seen that the B–N bond length in hexagon ring is increased from 1.45 Å to 1.48 Å (in range of $n = 1$-4) with increasing the number of B and N atoms (see Fig. 1). $B_{45}N_{45}H_{18}$ has a planar geometry with D_{3h} point group symmetry and $^1A_1$' electronic state (see Fig. 1f). Outwardly, the only difference from pristine GDY (see Fig. 1a) is that B and N atoms alternately replace C atoms in the framework. The atomic framework of $B_{45}N_{45}H_{18}$ can see to be BN hexagon interconnected by $B-N-B-N-B-N$ chains. B–N bond distances along the chain are following: 1.38, 1.28, 1.34, 1.28 and 1.38 Å. In contrast, B–N bond lengths in the BN hexagon are larger; with an average value of 1.48 Å. B–N bond lengths along the chains outside $B_{45}N_{45}H_{18}$ are larger than those of towards center. Besides, the longest BN bond in the optimized $B_{45}N_{45}H_{18}$ (pristine BNdiyne) is 1.48 Å, slightly larger than the calculated values of 1.42 Å (longest CC bond) in the optimized $C_{90}H_{18}$ (pristine GDY). Owing to these structural properties, the $B_{45}N_{45}H_{18}$ are so similar with $C_{90}H_{18}$. When parallelogram with a broken (green) line is plotted a unit cell, the lattice constant for $B_{45}N_{45}H_{18}$ is found to be $a_0 = 9.64$ and $b_0 = 9.62$ Å (see Fig. 1f). Compared with GDY, the lattice constant of $B_{45}N_{45}H_{18}$ is increased, this difference can be strong evidence of the presence of sp and sp^2 hybridization states between B and N atoms. These results agree well with the geometric characteristics predicted by periodic models [61–63]. We note that all the optimized models have no imaginary frequencies, indicating that these structures are stable.

The calculated binding energy per atom (E_b) for GDY and its BN analog models is plotted in Fig. 2 and tabulated in Table 1. The E_b value of $C_{90}H_{18}$ ($n = 0$) is calculated to be 7.64 eV, in excellent agreement with a value of 7.65 value [64]. Moreover, E_b decreases

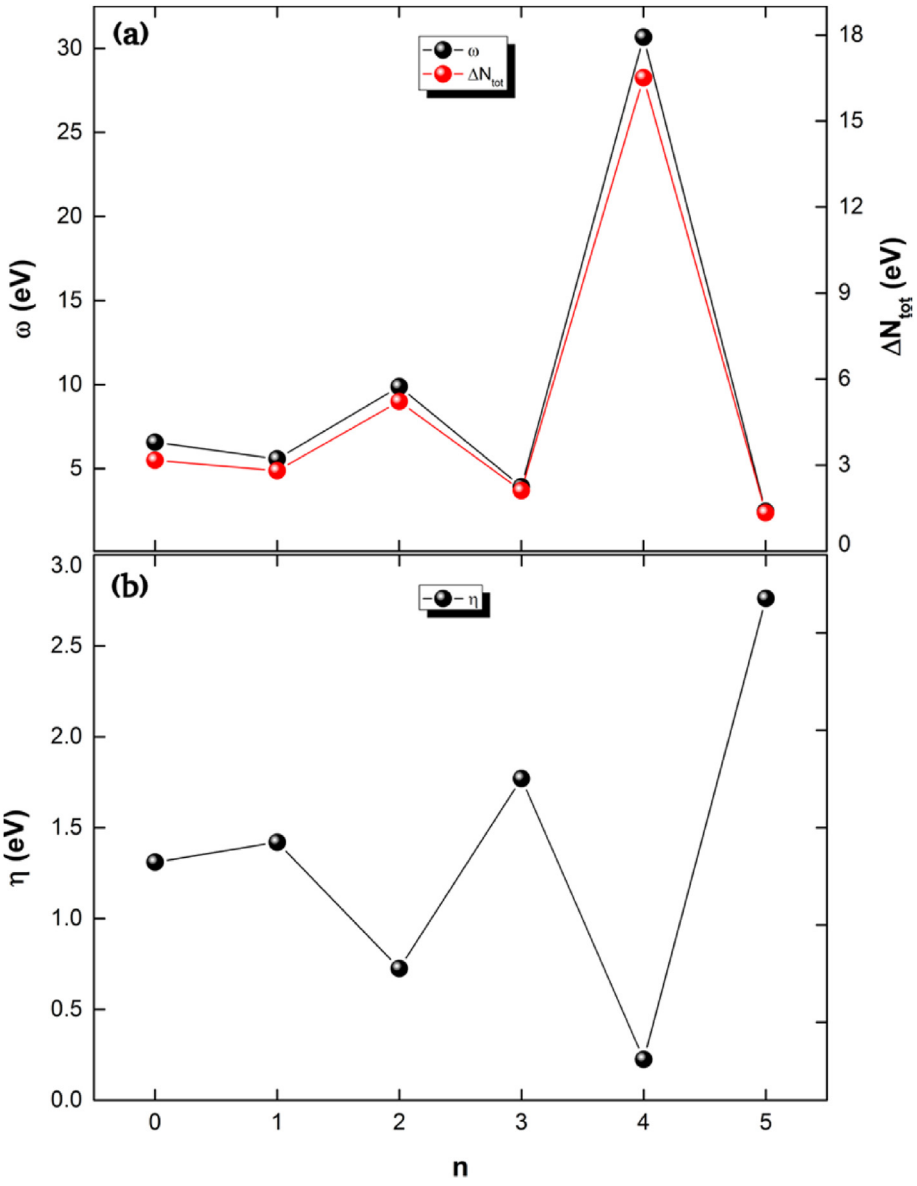

Fig. 5. (Colour online) Electrophilicity index (ω) and maximum amount electronic charge index (ΔN_{tot}) **(a)** and chemical hardness (η) **(b)** for $C_{90\text{-}18n}(BN)_{9n}H_{18}$ ($n = 0\text{-}5$) models. (For interpretation of the references to colour in this figure legend, the reader is referred to the Web version of this article.)

from 7.64 eV to 6.73 eV when B and N atoms are replaced with C atoms. This indicates that the pristine BNdiyne is less stable than pristine GDY. We also note that the GDY and BNdiyne models are less stable than graphene by about 0.31 and 1.22 eV/atom, which is in good agreement with previously predicted studies [65,66]. On the other hand, the formation energies (E_f) of GDY-like BN and BNdiyne models exhibit pronounced odd-even oscillation behavior are lie in the range of −0.08 and −1.40 kcal/mol (see Table 1).

Fig. 3 shows the density of states (DOS) and the HOMO-LUMO energy gap (E_g) of GDY and its BN analog models. The upper valence bands originate primarily from the states of C atoms in range of $n = 0\text{-}2$ (Fig. 3a–c). Besides, the lower valence bands are also derived from the states of N atoms after $n = 3$ (Fig. 3d–f). On the other hand, the conduction bands basically arise from the states of C atoms up to $n = 2$. Conversely, they are derived from the states of B atoms in range of $n = 3\text{-}5$. We note that decreases from when B and N atoms are replaced with C atoms.

The E_g shows an increasing/decreasing (i.e. a fluctuating) trend when B and N atoms are replaced with C atoms (see Fig. 4a). HOMO states increase significantly from −5.46 to −3.94 eV in range of $n = 0\text{-}4$, whereas LUMO states shift from −2.84 to −3.49 eV (see Figs. 3–4a). The E_g decreases significantly from 2.62 to 0.45 eV at $n = 4$ ($C_{18}B_{36}N_{36}H_{18}$). However, the HOMO and LUMO states of pristine BNdiyne (at $n = 5$) model shift to higher energies (see Fig. 3f), and thus E_g increases sharply up to 5.52 eV, indicating electrically an insulating behavior. This agrees extremely well with the values of 5.52 eV predicted for BNdiyne models [61]. In addition, the energy gap results obtained in the B3LYP functional are compared with HSE (in Table S7 as Supporting Information). These calculations show that HSE functional is in good agreement with B3LYP. It is interesting to note that the substitution causes a considerable shift in the relative position of the VB and CB. Our calculations indicate that the conductivity of $C_{18}B_{36}N_{36}H_{18}$ model is higher than that of the others. Comparing to the E_g of Si (1.14 eV), GaAs (1.43) and CdTe (1.5 eV) [67], $C_{18}B_{36}N_{36}H_{18}$ as a GDY-like BN model could be recommended as potential candidate and it could

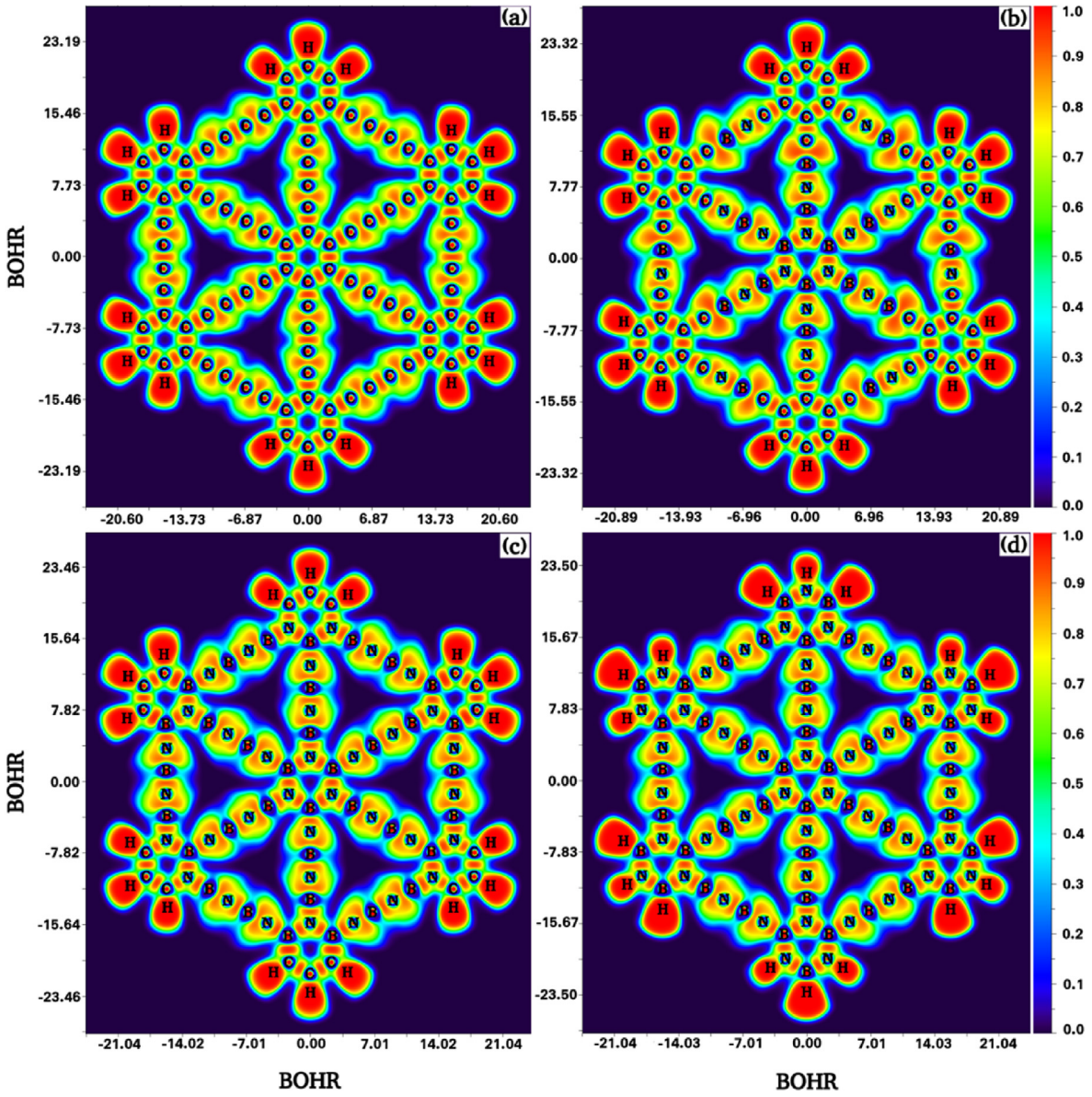

Fig. 6. (Colour online) Electron localization function (ELF) of $n = 0$ **(a)**, $n = 2$ **(b)**, $n = 4$ **(c)**, $n = 5$ **(d)** for $C_{90\text{-}18n}(BN)_{9n}H_{18}$ models. (For interpretation of the references to colour in this figure legend, the reader is referred to the Web version of this article.)

be used as an electron transport material as well as a suitable material for the possible use of chemical nanosensors.

The VIP of the pristine GDY (at $n = 0$) is calculated to be 6.20 eV (see Table 1). VIP shows a fluctuating and decreasing trend except $n = 1$ state (see Fig. 4b), whereas the pristine BNdiyne (at $n = 5$) displayed a clear peak with the substitution of the C atoms by B and N atoms. On the other hand, the VEA of the pristine GDY (at $n = 0$) is found to be 2.10 eV (see Table 1). The VEA shows a decreasing trend except $n = 2$ and 4 states, both have similar values, exhibiting odd-even oscillation behavior (see Fig. 4b). Besides, the graphs of ω and ΔN_{tot} show the similar trend with that of VEA. Also, the ω and ΔN_{tot} give a maximum at $n = 2$ and 4, indicating that high tendency to accept electron (see Fig. 5a). The η value of the pristine GDY ($n = 0$) is calculated to be 1.31 eV (see Table 1). With the substitution of the C atoms by B and N atoms, the η shows an increasing trend about 0.23–2.76 eV (see Fig. 5b). It can be seen that the plot of η exhibit generally the similar trend with that of VIP.

We carried out the electron localization function (ELF) analyses to evaluate the knowledge of the bond interaction (see Fig. 6). The ELF have a range of values between 0 and 1, where 0 and 1 values correspond to the absence of electrons and perfect localization, respectively [68]. The type of bond can become non-covalent because the reduction of ELF values causes less localization of electrons. The ELF values of bonds for $C_{90}H_{18}$ are found to be in the range of 0.9 and 1.0, which is in excellent agreement with previous study [69]. Similarly, the ELF values for GDY-like BN models ($n = 2, 4, 5$) are generally greater than 0.8 based on B and N atoms alternately replace C atoms. Note that electrons generally accumulated around N atoms rather than B atoms, and so they are held more tightly to N atoms. One reason is that because the N atom has a higher electronegativity than B. These results indicate the strong chemical covalent bonds which is in complete agreement with energetic and electronic results. We also note that the calculated ELF analyses indicate the stability of GDY-like BN models.

Fig. 7 shows the Wiberg bond index (WBI) of GDY and its BN analog models. The WBI is used to predict the bonding strength among C, B

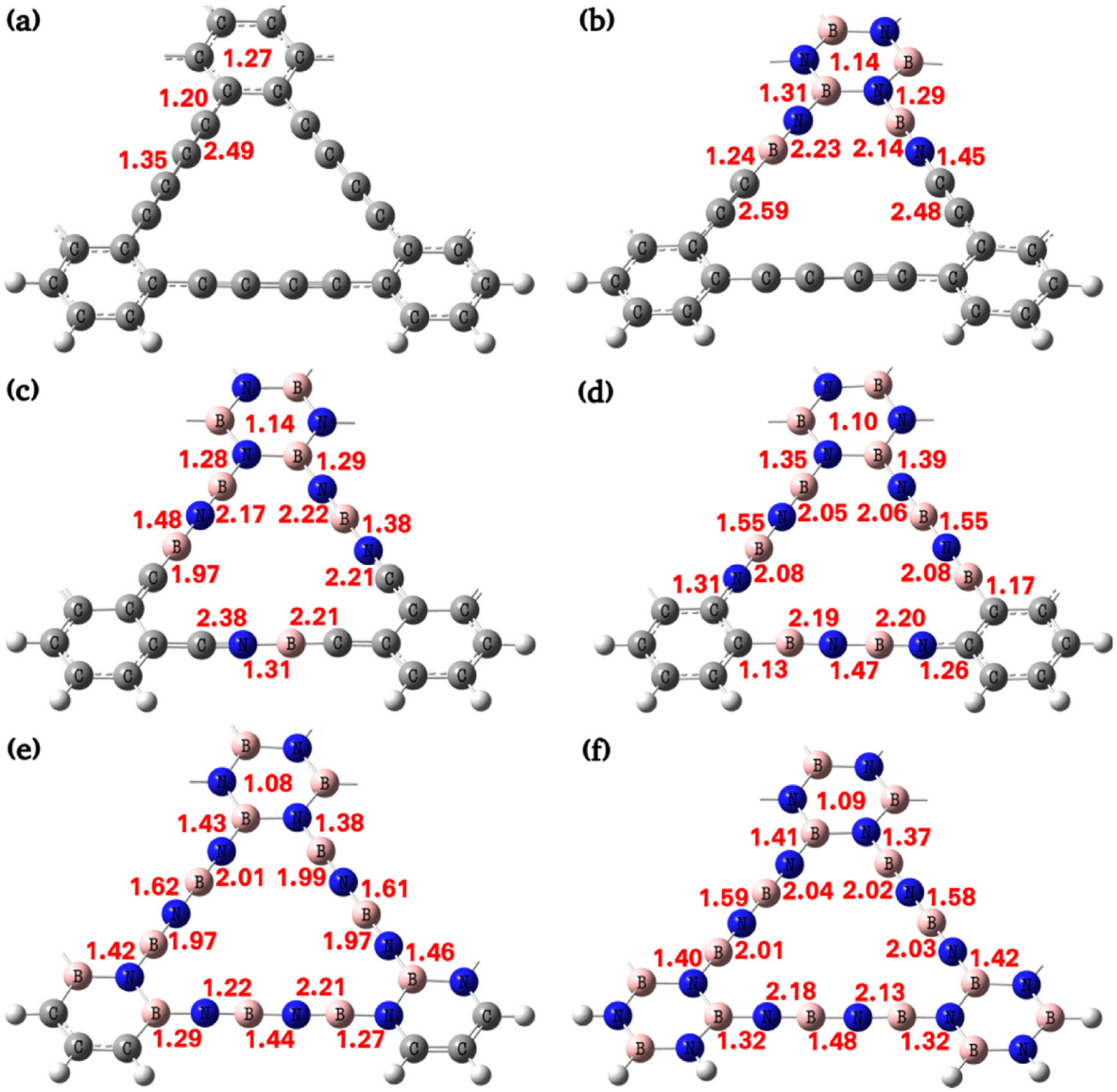

Fig. 7. (Colour online) Wiberg bond index (WBI) of $n = 0$ **(a)**, $n = 1$ **(b)**, $n = 2$ **(c)**, $n = 3$ **(d)**, $n = 4$ **(e)** and $n = 5$ **(f)** for $C_{90\text{-}18n}(BN)_{9n}H_{18}$ models. (For interpretation of the references to colour in this figure legend, the reader is referred to the Web version of this article.)

and N atoms, and so to assess the bonding characteristics of GDY and GDY-like BN models. For GDY (at $n = 0$), WBI for C–C bonds in the C hexagon is 1.27, which shows a single bond plus a delocalized p bond. WBI values for C–C bonds in the acetylene $C\cdots C{\equiv}C = C{\equiv}C\cdots C$ chains are also following: 1.20, 2.49, 1.35, 2.49 and 1.20 (see Fig. 7a). In the C–C interactions, the WBI values of the triple bonds are clearly larger than those of the single and double bonds. For $C_{72}B_9N_9H_{18}$ (at $n = 1$) model, the WBI for the BN hexagon is 1.14 (see Fig. 7b), indicating an almost single bond. However, the WBI values for B–N bonds in chains are in range of 1.29–1.31 and 2.14–2.23, which indicates single and double bonds, respectively. In addition, the WBI for C–C bonds in chains are about 2.48–2.59, which is typical triple bond. A similar trend can be seen in WBI values between B–N bonds with increasing the number of B and N atoms, whereas WBI values for the BN hexagons are slightly decreased (see Fig. 7c–f). Note that WBI for B–N bond in the center of the chain agrees extremely well with the values of 1.59 [61] predicted for pristine BNdiyne (see Fig. 7f). We should also mention that calculated WBI values are in compliance with the changes in bond lengths.

Next, we turn our attention to study the variation of the HOMO, LUMO, fermi energy levels and energy gap with temperature are shown in Fig. 8 for the GDY (n = 0) and GDY-like BN model (n = 4) sheet. Here, we compared the GDY with only for $n = 4$ which gives lowest energy gap value among all considered models (see Fig. 8a). For GDY sheet, the energy of the LUMO reduces from −3.476 eV to −3.791 eV, but the HOMO increases from −5.864 eV to −5.696 eV at 0 K and 1500 K, respectively (see Fig. 8b). Due to these changes, the value of the E_g slightly decreases up to about 1500 K due to increasing the intermolecular distance between C–C binary interactions and the lack of the symmetry in the chains of the GDY with temperature (see Fig. 8a). The decrease in the value of the E_g will give rise to an increase in the inhibition efficiency because the energy required to remove an electron from the last occupied orbital will be low [70]. On the other hand, after B and N doping, the value of LUMO decreases from −4.261 eV to −4.428 eV in the range of 0 K–1500 K for $n = 4$ (see Fig. 8c). However, interesting chemistry is predicted that HOMO energy shows an increasing trend with temperature. Therefore, we can conclude that

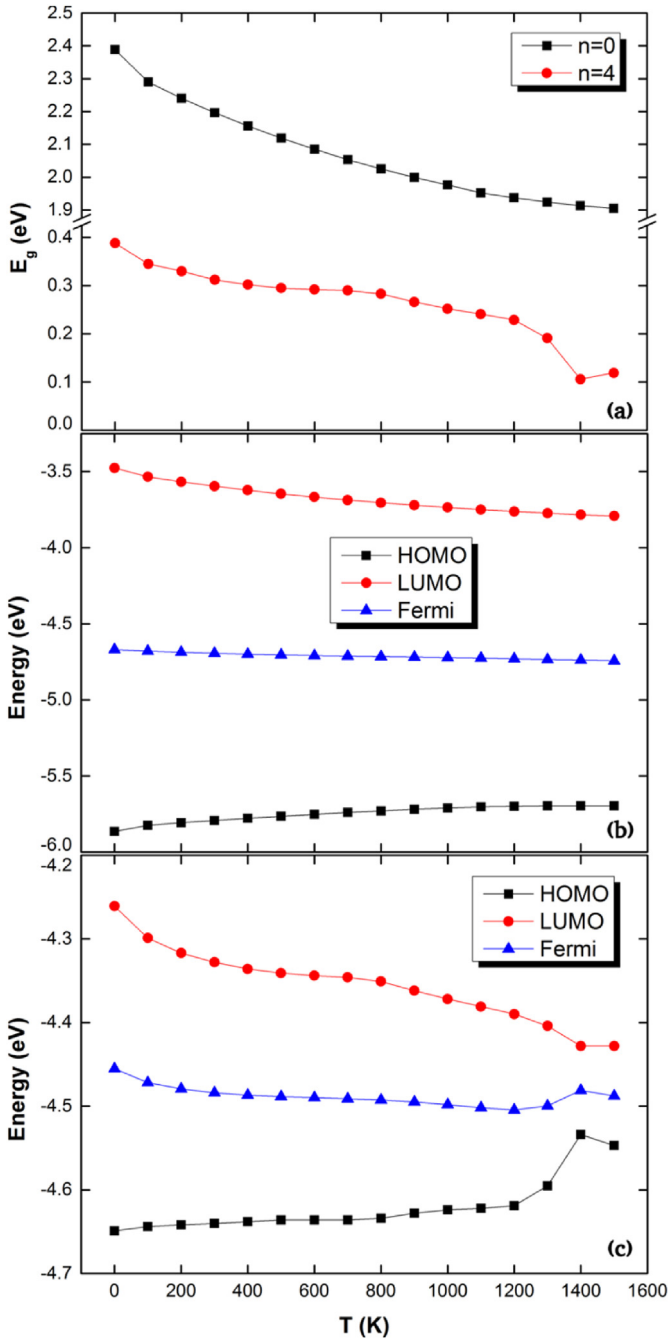

Fig. 8. (Colour online) The variations of energy gap (at $n = 0$ and 4) **(a)**, HOMO, LUMO and Fermi energy levels $n = 0$ **(b)** and $n = 4$ **(c)** depending on temperature for $C_{90-18n}(BN)_{9n}H_{18}$ models. (For interpretation of the references to colour in this figure legend, the reader is referred to the Web version of this article.)

the temperature for both cases causes a considerable shift in the relative position of the VB and CB. On the other hand, it is important to emphasize that a decrease in the value of the E_g is found for GDY (at $n = 0$) and GDY-like BN model (at $n = 4$) sheets (see Fig. 8a). It is interesting to note that after 1400 K, an increase in the E_g from 0.106 eV to 0.119 eV is calculated for $n = 4$ (see Fig. 8a), which can be attributed to the Burstein moss effect. When the temperature is increased, all states near the CB are being populated. The Fermi energy level is pushed higher from −4.481 eV at 1400 K to −4.487 eV at 1500 K (see Fig. 8c), hence temperature-induced considerable change in the band structure.

4. Conclusions

This study focuses on a structural transition from graphdiyne (GDY) to boron nitride (BN)-diyne and explores the effects of increasing the number of B and N atoms on structural, electronic and reactivity properties of GDY and its BN analog models ($C_{90-18n}(BN)_{9n}H_{18}$; $n = 0$-5) using DFT. It is found that a structural transition from quasi-planar geometry to planar geometry occurs in $C_{54}B_{18}N_{18}H_{18}$ (at $n = 2$). Moreover, we found that the stability decreases with increasing the number of B/N on GDY. In this case, the pristine GDY is found to be the most stable model with a value of 7.64 eV/atom, whereas the pristine BNdiyne is less stable than pristine GDY by about 0.92 eV/atom. The ELF analysis indicates that the electron density is higher at the positions occupied by N atoms. In addition, it confirms the B−N interactions in new BNdiyne sheets exhibit covalent bonding. It is interesting to note that the energy gap shows a increasing/decreasing trend in the wide range of 0.45−5.52 eV in terms of substitution of C atoms by B and N atoms. We note that the substitution causes a significantly shift in the relative position of the valence and conduction bands. The BNdiyne for $n = 5$ has the highest energy gap with a value of 5.52 eV, indicating an insulating character. However, $C_{18}B_{36}N_{36}H_{18}$ model with energy gap of 0.45 eV has higher conductivity than all models. Temperature induces a decrease in the energy gap for the GDY and BNdiyne (for $n = 4$). Therefore, new materials with desirable properties can be easily obtained by varying the number of the B/N atoms and temperature. The advantages of these stable BNdiyne models include 2D and porous structure, and so we believe that BNdiyne sheets will attract interest due to their porous texture and structure properties. Especially, they can be used in opto/nano-electronic as well as many technological applications ranging from drug carrier to energy storage. More importantly, our study provides new insight into the atomic engineering of BNdiyne models based on the content of the boron and nitrogen atoms.

CRediT authorship contribution statement

İskender Muz: Conceptualization, Methodology, Software, Validation, Formal analysis, Investigation, Resources, Data curation, Writing - original draft, Writing - review & editing, Visualization, Project administration. **Mustafa Kurban:** Methodology, Software, Validation, Formal analysis, Investigation, Resources, Data curation, Writing - original draft, Writing - review & editing, Supervision.

Declaration of competing interest

The authors declare that they have no known competing financial interests or personal relationships that could have appeared to influence the work reported in this paper.

Acknowledgements

The numerical calculations reported were partially performed at TUBITAK ULAKBIM, High Performance and Grid Computing Centre (TRUBA resources), Turkey.

Appendix A. Supplementary data

Supplementary data to this article can be found online at https://doi.org/10.1016/j.jallcom.2020.155987.

References

[1] M.M. Haley, S.C. Brand, J.J. Pak, Carbon networks based on dehydrobenzoannulenes: synthesis of graphdiyne substructures, Angew. Chem. Int.

Ed. 36 (1997) 836–838, https://doi.org/10.1002/anie.199708361.
[2] X. Gao, H. Liu, D. Wang, J. Zhang, Graphdiyne: synthesis, properties, and applications, Chem. Soc. Rev. 48 (2019) 908–936, https://doi.org/10.1039/c8cs00773j.
[3] S. Zhang, H. Du, J. He, C. Huang, H. Liu, G. Cui, Y. Li, Nitrogen-doped graphdiyne applied for lithium-ion storage, ACS Appl. Mater. Interfaces 8 (2016) 8467–8473, https://doi.org/10.1021/acsami.6b00255.
[4] S. Wang, L. Yi, J.E. Halpert, X. Lai, Y. Liu, H. Cao, R. Yu, D. Wang, Y. Li, A novel and highly efficient photocatalyst based on P25-graphdiyne nanocomposite, Small 8 (2012) 265–271, https://doi.org/10.1002/smll.201101686.
[5] C. Sun, D.J. Searles, Lithium storage on graphdiyne predicted by DFT calculations, J. Phys. Chem. C 116 (2012) 26222–26226, https://doi.org/10.1021/jp309638z.
[6] A. Farokh Niaei, T. Hussain, M. Hankel, D. Searles, Sodium-intercalated bulk graphdiyne as an anode material for rechargeable batteries, J. Power Sources 343 (2017) 354–363, https://doi.org/10.1016/jjpowsour.2017.01.027.
[7] Y. Jiao, A. Du, M. Hankel, Z. Zhu, V. Rudolph, S.C. Smith, Graphdiyne: a versatile nanomaterial for electronics and hydrogen purification, Chem. Commun. 47 (2011) 11843–11845, https://doi.org/10.1039/C1CC15129K.
[8] M. Zhang, X. Wang, H. Sun, N. Wang, Q. Lv, W. Cui, Y. Long, C. Huang, Enhanced paramagnetism of mesoscopic graphdiyne by doping with nitrogen, Sci. Rep. 7 (2017) 11535, https://doi.org/10.1038/s41598-017-11698-9.
[9] J. He, S.Y. Ma, P. Zhou, C.X. Zhang, C. He, L.Z. Sun, Magnetic properties of single transition-metal atom absorbed graphdiyne and graphyne sheet from DFT plus U calculations, J. Phys. Chem. C 116 (2012) 26313–26321, https://doi.org/10.1021/jp307408u.
[10] G. Li, Y. Li, H. Liu, Y. Guo, Y. Li, D. Zhu, Architecture of graphdiyne nanoscale films, Chem. Commun. 46 (2010) 3256–3258, https://doi.org/10.1039/B922733D.
[11] M. Long, L. Tang, D. Wang, Y. Li, Z. Shuai, Electronic structure and carrier mobility in graphdiyne sheet and nanoribbons: theoretical predictions, ACS Nano 5 (2011) 2593–2600, https://doi.org/10.1021/nn102472s.
[12] V. Nagarajan, R. Chandiramouli, Investigation of NH 3 adsorption behavior on graphdiyne nanosheet and nanotubes: a first-principles study, J. Mol. Liq. 249 (2018) 24–32, https://doi.org/10.1016/j.molliq.2017.11.007.
[13] L. Sun, P.H. Jiang, H.J. Liu, D.D. Fan, J.H. Liang, J. Wei, L. Cheng, J. Zhang, J. Shi, Graphdiyne, A two-dimensional thermoelectric material with high figure of merit, Carbon N. Y. 90 (2015) 255–259, https://doi.org/10.1016/j.carbon.2015.04.037.
[14] C. Lu, Y. Yang, J. Wang, R. Fu, X. Zhao, L. Zhao, Y. Ming, Y. Hu, H. Lin, X. Tao, Y. Li, W. Chen, High-performance graphdiyne-based electrochemical actuators, Nat. Commun. 9 (2018) 752, https://doi.org/10.1038/s41467-018-03095-1.
[15] K. Krishnamoorthy, S. Thangavel, J.C. Veetil, N. Raju, G. Venugopal, S.J. Kim, Graphdiyne nanostructures as a new electrode material for electrochemical supercapacitors, Int. J. Hydrogen Energy 41 (2016) 1672–1678, https://doi.org/10.1016/j.ijhydene.2015.10.118.
[16] H. Shang, Z. Zuo, Y. Li, Highly lithiophilic graphdiyne nanofilm on 3D free-standing Cu nanowires for high-energy-density electrodes, ACS Appl. Mater. Interfaces 11 (2019) 17678–17685, https://doi.org/10.1021/acsami.9b03633.
[17] J. Kim, S. Kang, J. Lim, W.Y. Kim, Study of Li adsorption on graphdiyne using hybrid DFT calculations, ACS Appl. Mater. Interfaces 11 (2019) 2677–2683, https://doi.org/10.1021/acsami.8b03482.
[18] L. Li, Z. Zuo, H. Shang, F. Wang, Y. Li, In-situ constructing 3D graphdiyne as all-carbon binder for high-performance silicon anode, Nano Energy 53 (2018) 135–143, https://doi.org/10.1016/j.nanoen.2018.08.039.
[19] S. Thangavel, K. Krishnamoorthy, V. Krishnaswamy, N. Raju, S.J. Kim, G. Venugopal, Graphdiyne-ZnO nanohybrids as an advanced photocatalytic material, J. Phys. Chem. C 119 (2015) 22057–22065, https://doi.org/10.1021/acs.jpcc.5b06138.
[20] S. Pari, A. Cuéllar, B.M. Wong, Structural and electronic properties of graphdiyne carbon nanotubes from large-scale DFT calculations, J. Phys. Chem. C 120 (2016) 18871–18877, https://doi.org/10.1021/acs.jpcc.6b05265.
[21] I. Muz, M. Kurban, A comprehensive study on electronic structure and optical properties of carbon nanotubes with doped B, Al, Ga, Si, Ge, N, P and as and different diameters, J. Alloys Compd. 802 (2019) 25–35, https://doi.org/10.1016/j.jallcom.2019.06.210.
[22] İ. Muz, F. Göktaş, M. Kurban, 3d-transition metals (Cu, Fe, Mn, Ni, V and Zn)-doped pentacene π-conjugated organic molecule for photovoltaic applications: DFT and TD-DFT calculations, Theor. Chem. Acc. 139 (2020) 23, https://doi.org/10.1007/s00214-020-2544-9.
[23] İ. Muz, M. Kurban, M. Dalkilic, DFT and TD-DFT studies of new pentacene-based organic molecules as a donor material for bulk-heterojunction solar cells, J. Comput. Electron. 19 (2020), https://doi.org/10.1007/s10825-020-01493-7.
[24] İ. Muz, M. Atiş, Boron-doped hydrogenated Al 3 clusters: a material for hydrogen storage, J. Alloys Compd. 667 (2016) 275–281, https://doi.org/10.1016/j.jallcom.2016.01.151.
[25] İ. Muz, M. Kurban, Enhancement of electronic, photophysical and optical properties of 5,5′-Dibromo-2,2′-bithiophene molecule: new aspect to molecular design, Opto-Electron. Rev. 27 (2019) 113–118, https://doi.org/10.1016/j.opelre.2019.03.002.
[26] Z. Zheng, X. Wang, W. Mi, Electric field tunable electronic structure in two dimensional van der Waals g-C2N/XSe2(X = Mo, W) heterostructures, Carbon N. Y. 117 (2017) 393–398, https://doi.org/10.1016/j.carbon.2017.03.018.
[27] J. Mahmood, E.K. Lee, M. Jung, D. Shin, I.Y. Jeon, S.M. Jung, H.J. Choi, J.M. Seo, S.Y. Bae, S.D. Sohn, N. Park, J.H. Oh, H.J. Shin, J.B. Baek, Nitrogenated holey two-dimensional structures, Nat. Commun. 6 (2015) 1–7, https://doi.org/10.1038/ncomms7486.
[28] J.S. Lee, X. Wang, H. Luo, S. Dai, Fluidic carbon precursors for formation of functional carbon under ambient pressure based on ionic liquids, Adv. Mater. 22 (2010) 1004–1007, https://doi.org/10.1002/adma.200903403.
[29] Z.D. Zheng, X.C. Wang, W.B. Mi, Tunable electronic structure of monolayer semiconductor g-C 2 N by adsorbing transition metals: a first-principles study, Carbon N. Y. 109 (2016) 764–770, https://doi.org/10.1016/j.carbon.2016.08.088.
[30] S. Guan, Y. Cheng, C. Liu, J. Han, Y. Lu, S.A. Yang, Y. Yao, Effects of strain on electronic and optic properties of holey two-dimensional C 2 N crystals, Appl. Phys. Lett. 107 (2015), 231904, https://doi.org/10.1063/1.4937269.
[31] A. Thomas, A. Fischer, F. Goettmann, M. Antonietti, J.-O. Müller, R. Schlögl, J.M. Carlsson, Graphitic carbon nitride materials: variation of structure and morphology and their use as metal-free catalysts, J. Mater. Chem. 18 (2008) 4893, https://doi.org/10.1039/b800274f.
[32] S.-S. Yu, W.-T. Zheng, Effect of N/B doping on the electronic and field emission properties for carbon nanotubes, carbon nanocones, and graphene nanoribbons, Nanoscale 2 (2010) 1069–1082, https://doi.org/10.1039/c0nr00002g.
[33] B.K. Jiang, A.Y. Chen, J.F. Gu, J.T. Fan, Y. Liu, P. Wang, H.J. Li, H. Sun, J.H. Yang, X.Y. Wang, Corrosion resistance enhancement of magnesium alloy by N-doped graphene quantum dots and polymethyltrimethoxysilane composite coating, Carbon N. Y. 157 (2020) 537–548, https://doi.org/10.1016/j.carbon.2019.09.013.
[34] Y. Li, W. Ma, J. Sun, M. Lin, Y. Niu, X. Yang, Y. Xu, Electrochemical generation of Fe3C/N-doped graphitic carbon nanozyme for efficient wound healing in vivo, Carbon N. Y. 159 (2020) 149–160, https://doi.org/10.1016/j.carbon.2019.11.093.
[35] X. Qin, Y. Huang, K. Wang, T. Xu, S. Li, M. Zhao, Y. Wang, Q. Chen, Novel hexagonal Bi2O2CO3 porous nanoplate/nitrogen-doped graphene nanomaterials with enhanced electrochemical properties for oxygen reduction reaction in acidic media for fuel cells, Carbon N. Y. 152 (2019) 459–473, https://doi.org/10.1016/j.carbon.2019.06.028.
[36] N. Wanninayake, Q. Ai, R. Zhou, M.A. Hoque, S. Herrell, M. Guzman I, C. Risko, D.Y. Kim, Understanding the effect of host structure of nitrogen doped ultrananocrystalline diamond electrode on electrochemical carbon dioxide reduction, Carbon N. Y. 157 (2020) 408–419, https://doi.org/10.1016/j.carbon.2019.10.022.
[37] M. Kurban, Electronic structure, optical and structural properties of Si, Ni, B and N-doped a carbon nanotube: DFT study, Optik 172 (2018) 295–301, https://doi.org/10.1016/j.ijleo.2018.07.028.
[38] H. Shang, Z. Zuo, H. Zheng, K. Li, Z. Tu, Y. Yi, H. Liu, Y. Li, Y. Li, N-doped graphdiyne for high-performance electrochemical electrodes, Nano Energy 44 (2018) 144–154, https://doi.org/10.1016/j.nanoen.2017.11.072.
[39] X. Shen, Z. Yang, K. Wang, N. Wang, J. He, H. Du, C. Huang, Nitrogen-doped graphdiyne as high-capacity electrode materials for both lithium-ion and sodium-ion capacitors, ChemElectroChem 5 (2018) 1435–1443, https://doi.org/10.1002/celc.201800300.
[40] Q. Lv, W. Si, J. He, L. Sun, C. Zhang, N. Wang, Z. Yang, X. Li, X. Wang, W. Deng, Y. Long, C. Huang, Y. Li, Selectively nitrogen-doped carbon materials as superior metal-free catalysts for oxygen reduction, Nat. Commun. 9 (2018) 3376, https://doi.org/10.1038/s41467-018-05878-y.
[41] Q. Lv, W. Si, Z. Yang, N. Wang, Z. Tu, Y. Yi, C. Huang, L. Jiang, M. Zhang, J. He, Y. Long, Nitrogen-doped porous graphdiyne: a highly efficient metal-free electrocatalyst for oxygen reduction reaction, ACS Appl. Mater. Interfaces 9 (2017) 29744–29752, https://doi.org/10.1021/acsami.7b08115.
[42] Y. Ma, J. Lin, X.-N. Song, C.-K. Wang, W. Hua, Y. Luo, Local structures of nitrogen-doped graphdiynes determined by computational X-ray spectroscopy, Carbon N. Y. 149 (2019) 672–678, https://doi.org/10.1016/j.carbon.2019.04.045.
[43] I. Muhammad, S. Wang, J. Liu, H. Xie, Q. Sun, Boron-graphdiyne as an anode material for Li, Na, and K ion batteries with high capacities and low diffusion barriers, J. Renew. Sustain. Energy 11 (2019) 14106, https://doi.org/10.1063/1.5079928.
[44] S. Grimme, A. Hansen, J.G. Brandenburg, C. Bannwarth, Dispersion-corrected mean-field electronic structure methods, Chem. Rev. 116 (2016) 5105–5154, https://doi.org/10.1021/acs.chemrev.5b00533.
[45] M.J. Frisch, G.W. Trucks, H.B. Schlegel, G.E. Scuseria, M.A. Robb, J.R. Cheeseman, G. Scalmani, V. Barone, B. Mennucci, G.A. Petersson, H. Nakatsuji, M. Caricato, X. Li, H.P. Hratchian, A.F. Izmaylov, J. Bloino, G. Zheng, J.L. Sonnenberg, M. Hada, M. Ehara, K. Toyota, R. Fukuda, J. Hasegawa, M. Ishida, T. Nakajima, Y. Honda, O. Kitao, H. Nakai, T. Vreven, J.A. Montgomery, J.E. Peralta, F. Ogliaro, M. Bearpark, J.J. Heyd, E. Brothers, K.N. Kudin, V.N. Staroverov, R. Kobayashi, J. Normand, K. Raghavachari, A. Rendell, J.C. Burant, S.S. Iyengar, J. Tomasi, M. Cossi, N. Rega, J.M. Millam, M. Klene, J.E. Knox, J.B. Cross, V. Bakken, C. Adamo, J. Jaramillo, R. Gomperts, R.E. Stratmann, O. Yazyev, A.J. Austin, R. Cammi, C. Pomelli, J.W. Ochterski, R.L. Martin, K. Morokuma, V.G. Zakrzewski, G.A. Voth, P. Salvador, J.J. Dannenberg, S. Dapprich, A.D. Daniels, Farkas, J.B. Foresman, J. V Ortiz, J. Cioslowski, D.J. Fox, Gaussian 09, Revision E.01, Gaussian Inc., Wallingford CT, 2009.
[46] A.D. Becke, A new mixing of hartree-fock and local density functional theories, J. Chem. Phys. 98 (1993) 1372–1377, https://doi.org/10.1063/1.464304.
[47] N.M. O'Boyle, A.L. Tenderholt, K.M. Langner, CCLIB: A library for package-

independent computational chemistry algorithms, J. Comput. Chem. 29 (2008) 839–845, https://doi.org/10.1002/jcc.20823.
[48] T. Lu, F. Chen, Multiwfn: a multifunctional wavefunction analyzer, J. Comput. Chem. 33 (2012) 580–592, https://doi.org/10.1002/jcc.22885.
[49] R. Dennington, T.A. Keith, J.M. Millam, GaussView, Version 5. Semichem Inc., Shawnee Mission, KS. (2009).
[50] B. Aradi, B. Hourahine, T. Frauenheim, DFTB+, a sparse matrix-based implementation of the DFTB method, J. Phys. Chem. 111 (2007) 5678–5684, https://doi.org/10.1021/jp070186p.
[51] V.Q. Vuong, J.A. Kuriappan, M. Kubillus, J.J. Kranz, T. Mast, T.A. Niehaus, S. Irle, M. Elstner, Parametrization and benchmark of long-range corrected DFTB2 for organic molecules, J. Chem. Theor. Comput. 14 (2018) 115–125, https://doi.org/10.1021/acs.jctc.7b00947.
[52] B. Lukose, A. Kuc, J. Frenzel, T. Heine, On the reticular construction concept of covalent organic frameworks, Beilstein J. Nanotechnol. 1 (2010) 60–70, https://doi.org/10.3762/bjnano.1.8.
[53] H.C. Andersen, Molecular-dynamics simulations at constant pressure and-or temperature, J. Chem. Phys. 72 (1980) 2384–2393, https://doi.org/10.1063/1.439486.
[54] L. Verlet, Computer “Experiments” on classical fluids. I. thermodynamical properties of Lennard-Jones molecules, Phys. Rev. 159 (1967) 98–103, https://doi.org/10.1103/PhysRev.159.98.
[55] A. Seif, M.J. López, A. Granja-DelRío, K. Azizi, J.A. Alonso, Adsorption and growth of palladium clusters on graphdiyne, Phys. Chem. Chem. Phys. 19 (2017) 19094–19102, https://doi.org/10.1039/C7CP03263C.
[56] N. Narita, S. Nagai, S. Suzuki, K. Nakao, Optimized geometries and electronic structures of graphyne and its family, Phys. Rev. B 58 (1998) 11009–11014, https://doi.org/10.1103/PhysRevB.58.11009.
[57] Y. Pei, Mechanical properties of graphdiyne sheet, Phys. B Condens. Matter 407 (2012) 4436–4439, https://doi.org/10.1016/j.physb.2012.07.026.
[58] S. Jalili, F. Houshmand, J. Schofield, Study of carrier mobility of tubular and planar graphdiyne, Appl. Phys. A 119 (2015) 571–579, https://doi.org/10.1007/s00339-015-8992-8.
[59] M. Ebadi, A. Reisi-Vanani, F. Houshmand, P. Amani, Calcium-decorated graphdiyne as a high hydrogen storage medium: evaluation of the structural and electronic properties, Int. J. Hydrogen Energy 43 (2018) 23346–23356, https://doi.org/10.1016/j.ijhydene.2018.10.205.
[60] Z. Lu, S. Li, P. Lv, C. He, D. Ma, Z. Yang, First principles study on the interfacial properties of NM/graphdiyne (NM = Pd, Pt, Rh and Ir): the implications for NM growing, Appl. Surf. Sci. 360 (2016) 1–7, https://doi.org/10.1016/j.apsusc.2015.10.219.
[61] H. Li, W. Fu, K. Xu, C. Wang, Y. Li, J. Zhang, W. Jiang, W. Zhu, H. Li, The electronic structure and physicochemical property of boron nitridene, J. Mol. Graph. Model. 94 (2020), https://doi.org/10.1016/j.jmgm.2019.107475.
[62] X.-D. Li, X.-L. Cheng, Predicting the structural and electronic properties of two-dimensional single layer boron nitride sheets, Chem. Phys. Lett. 694 (2018) 102–106, https://doi.org/10.1016/j.cplett.2018.01.043.
[63] Z. Yang, Y. Zhang, M. Guo, J. Yun, Adsorption of hydrogen and oxygen on graphdiyne and its BN analog sheets: a density functional theory study, Comput. Mater. Sci. 160 (2019) 197–206, https://doi.org/10.1016/j.commatsci.2018.12.033.
[64] H. Bu, M. Zhao, A. Wang, X. Wang, First-principles prediction of the transition from graphdiyne to a superlattice of carbon nanotubes and graphene nanoribbons, Carbon N. Y. 65 (2013) 341–348, https://doi.org/10.1016/j.carbon.2013.08.035.
[65] N. Narita, S. Nagai, S. Suzuki, K. Nakao, Electronic structure of three-dimensional graphyne, Phys. Rev. B 62 (2000) 11146–11151, https://doi.org/10.1103/PhysRevB.62.11146.
[66] A.N. Enyashin, A.L. Ivanovskii, Graphene allotropes, Phys. Status Solidi B 248 (2011) 1879–1883, https://doi.org/10.1002/pssb.201046583.
[67] B. Streetman, S. Banerjee, Solid State Electronic Devices, fifth ed., Prentice Hall, Upper Saddle River, N.J., 2000.
[68] B. Silvi, A. Savin, Classification of chemical-bonds based on topological analysis of electron localization functions, Nature 371 (1994) 683–686, https://doi.org/10.1038/371683a0.
[69] B. Mortazavi, M. Makaremi, M. Shahrokhi, Z. Fan, T. Rabczuk, N-graphdiyne two-dimensional nanomaterials: semiconductors with low thermal conductivity and high stretchability, Carbon N. Y. 137 (2018) 57–67, https://doi.org/10.1016/j.carbon.2018.04.090.
[70] G. Gece, Theoretical evaluation of the inhibition properties of two thiophene derivatives on corrosion of carbon steel in acidic media, Mater. Corros. Und Korrosion. 64 (2013) 940–944, https://doi.org/10.1002/maco.201106482.